*Article*

# Sustainable and Regenerable Alkali Metal-Containing Carbons Derived from Seaweed for CO$_2$ Post-Combustion Capture

**Antonio Salituro \*, Aidan Westwood, Andrew Ross and Richard Brydson**

School of Chemical and Process Engineering, University of Leeds, Leeds, LS2 9JT, UK;
a.v.k.westwood@leeds.ac.uk (A.W.); a.b.ross@leeds.ac.uk (A.R.); r.m.drummond-brydson@leeds.ac.uk (R.B.)
\* Correspondence: orsettodelkent@gmail.com

**Abstract:** Alkali-based CO$_2$ sorbents were prepared from a novel material (i.e., *Laminaria hyperborea*). The use of this feedstock, naturally containing alkali metals, enabled a simple, green and low-cost route to be pursued. In particular, raw macroalgae was pyrolyzed at 800 °C. The resulting biochar was activated with either CO$_2$ or KOH. KOH–activated carbon (AC) had the largest surface area and attained the highest CO$_2$ uptake at 35 °C and 1 bar. In contrast, despite much lower porosity, the seaweed-derived char and its CO$_2$-activated counterpart outweighed the CO$_2$ sorption performance of KOH–AC and commercial carbon under simulated post-combustion conditions (53 °C and 0.15 bar). This was ascribed to the greater basicity of char and CO$_2$–AC due to the presence of alkali metal-based functionalities (i.e., MgO) within their structure. These were responsible for a sorption of CO$_2$ at lower partial pressure and higher temperature. In particular, the CO$_2$–AC exhibited fast sorption kinetics, facile regeneration and good durability over 10 working cycles. Results presented in the current article will be of help for enhancing the design of sustainable alkali metal-containing CO$_2$ captors.

**Keywords:** alkali metals; carbon; CO$_2$ sorption; green sorbents; *Laminaria hyperborea*; post-combustion

## 1. Introduction

Today the greenhouse effect is a well-known issue, which is a continuous matter of discussion in the scientific community. CO$_2$ is widely recognized as one of the most relevant greenhouse gases (GHGs). At present, its emissions are mainly due to the use of unrenewable energy sources (fossil fuels) such as coal, employed in stationary power plants for electricity generation, and oil, the derivatives of which are used for motor transport [1]. Due to the progressive increase in the CO$_2$ level affecting the atmosphere, the global surface temperature has already increased by 0.8 °C in the 20th Century, and is expected to rise further by 1.4–5.8 °C during the 21$^{st}$ Century [2].

Several carbon capture technologies have been proposed in recent years. At present, the post-combustion route, with specific regard to chemical absorption onto amines, still represents the most ready-to-use approach in the industrial context [3]. This is because post-combustion technology can easily be retrofitted into existing plants. Nevertheless, the use of amine-based solvents poses various disadvantages [4,5]. These include the energy penalty due to the excessive amount of heat required for solvent regeneration, the corrosion affecting the reactor and the amine degradation over more working cycles. For all of these reasons, this technology has not yet been implemented on an industrial scale.

Therefore, the research community has directed its attention towards alternative post-combustion technologies for CO$_2$ capture. Adsorption onto solid materials is a focus of this research. Carbons are one of the most efficient types of sorbents among those available on the market (e.g., zeolites, metal organic

frameworks (MOFs), etc.) [6]. Nonetheless, the $CO_2$ sorption performance of virgin activated carbons is adversely affected by higher temperature [7] and lower gas partial pressure [8], which are representative of post-combustion conditions. In fact, in a typical coal-fired power plant, $CO_2$ capture treatment would normally be conducted after flue gas desulfurization (FGD). At this stage, the gas stream is usually at ca. 50 °C and features low carbon dioxide concentrations (10–14%) [9]. Under these conditions, the effect of basicity becomes more important in ensuring a selective sorption of $CO_2$, as the effectiveness of the physisorption mechanism is dramatically reduced. Accordingly, successful attempts at increasing the selectivity of the parent activated carbons under post-combustion conditions were achieved by using carbons as a substrate for amine impregnation [10,11]. However, amine-functionalization inevitably implies an extra step for the preparation of the $CO_2$ chemisorbents, thus involving a longer and costly production process. Furthermore, amino groups tend to leach from the solid support during cyclic regeneration, thereby reducing their capture potential over time [12] and implying the release of compounds that are harmful to the environment. As an alternative to the use of amine-doped solid materials, alkali metal-containing sorbents [13–16] could be applied for post-combustion capture of $CO_2$. On the other hand, methods for the preparation of alkali metal-based sorbents reported in the literature are not environmentally friendly, as chemicals are required. In addition to this, manufacturing techniques are complex and expensive due to the application of several energy intensive treatments. A series of studies on the use of seaweed for $CO_2$-activated carbon production has been recently published. Ding and Yangxian [17] generated seaweed (*Sargassum* and *Enteromorpha*) porous biochars using a single step KOH activation. Both textural properties and surface chemistry (oxygen-containing functional groups) of sorbents were investigated. However, the study did not infer which factor predominantly affected $CO_2$ adsorption. *Sargassum horneri*-based activated carbons were synthesized by Zeng et al. [18]. Although the high nitrogen content (3.56 wt.%) measured for the algae-derived activated carbons was reported to favor $CO_2$ adsorption, $CO_2$ capture potential was primarily ascribed to the presence of abundant narrow micropores. The same conclusion was reported by Balamar et al. [19], who fabricated $CO_2$ sorbents by applying KOH activation directly on raw seaweed (*Sargassum fusiforme*). In all the above-mentioned works, the intrinsic alkalinity of the precursor seaweed and its effect on its performance as a $CO_2$-absorber were not considered.

Hence, in view of the points aforementioned, the present work aimed to do the following:

- prepare green $CO_2$ sorbents starting from a novel and widely available feedstock, i.e., *Laminaria hyperborea*, whose intrinsic high alkalinity should allow the study of this property on $CO_2$ absorption;
- identify the best (low-cost and environmentally sound process, i.e., no chemical addition) activation route to produce reusable $CO_2$ sorbents with high alkalinity.

## 2. Materials and Methods

### 2.1. Activated Carbon Preparation

*Laminaria hyperborea* was collected from Clachan Sound, West Scotland, in the summer season (July). Raw material, defined as LH_S, was water washed in distilled water, air-dried and ground prior to further treatment. Around 5 g of raw seaweed was pyrolyzed under $N_2$ (flow rate of 100 mL·min$^{-1}$) at 800 °C for 1 h in a horizontal tube furnace at a heating rate of ca. 25 °C·min$^{-1}$. Char, denoted as LH_S800, was then subjected to two different thermochemical process routes (see Figure 1). The first process route, i.e., $CO_2$ activation, was performed by heating the char up to 700 °C according to a heating rate of 10 °C·min$^{-1}$. The char was then isothermally held for 30 min. $CO_2$ (flow rate of 0.6 L·min$^{-1}$) flowed throughout the heating treatment. The second treatment, i.e., KOH activation, entailed mixing char and KOH pellets (Sigma Aldrich, P1767) in a mortar in a 1:4 ratio. Then the char/KOH dry mixture was heated up to 750 °C under $N_2$ (flow rate of 100 mL·min$^{-1}$) at a heating rate of 5 °C·min$^{-1}$. Activation temperature was held for 1 h. Following heat-treatment, carbon was sequentially washed with distilled water and 1 M HCl (VWR International, 20252.420) in order

to remove any residual potassium-based compounds. $CO_2$ and KOH activation conditions were those that maximized the Brunauer–Emmett–Teller (BET) surface area of the final carbons. $CO_2$ and KOH-activated chars are referred as LH_S800PA and LH_S800CA, respectively.
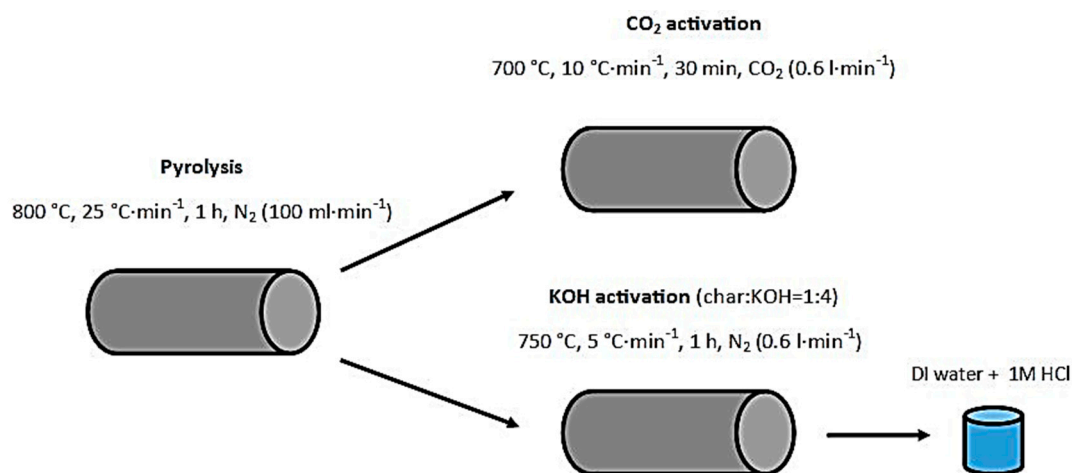


**Figure 1.** Schematic of experimental routes for the production of *Laminaria hyperborea*–derived activated carbons.

Yields obtained for LH_800, LH_S800PA and LH_S800CA are given in Table S3, Supplementary Materials.

Commercial carbon (designated as AR) was supplied by Chemviron Carbon. Magnesium oxide (cat no. CHE2450) was purchased from Scientific Laboratory Supplies (SLS) Ltd. (Nottingham, UK).

Details of materials produced and used in this study are given in Table 1.

**Table 1.** Details about materials produced.

| Sample ID | Material Type | Process Conditions |
|---|---|---|
| LH_S | Raw seaweed | N/A |
| LH_S800 | Pyrolyzed char | 800 °C, 60 min, $N_2$ |
| LH_S800PA | $CO_2$-activated carbon | 700 °C, 30 min, $CO_2$ |
| LH_S800CA | KOH-activated carbon | 750 °C, 60 min, $N_2$, char:KOH ratio =1:4 |
| AR | Commercial activated carbon | N/A |
| MgO | Magnesium oxide | N/A |

N/A stands for not applicable.

## 2.2. Activated Carbon Characterization

Measurement of $N_2$ adsorption isotherms was performed on a Quantachrome Autosorb 1C gas sorption analyzer. A relative pressure ($P/P_0$) ranging between approximately $10^{-3}$ and 0.99 was considered. Surface areas were calculated by applying the Brunauer–Emmett–Teller (BET) model [20] to the $N_2$ adsorption data over the $P/P_0$ range recommended by ISO-FDIS 9277:2010 [21]. Gurvitsch's rule ($P/P_0 = 0.99$) [22] was applied for the estimation of total pore volume. Micropore volumes were determined by using the Dubinin–Radushkevich (DR) model ($P/P_0 < 0.02$) [23], whereas mesoporous volumes were obtained from integration of the Barrett–Joyner–Halenda (BJH) distribution (2 < pore diameter (d) < 50 nm). Ultimate analyses were carried out with the use of an elemental analyzer (Flash EA2000), while proximate analyses were performed by using either the British Standards Institution (BSI) procedure [24–26] or thermogravimetric analysis (TGA). The morphology of materials was examined with the aid of an EVO MA15 scanning electron microscope (SEM), which was operated

with a working distance of 8 to 9 mm and an accelerating voltage of 20 kV using the in-lens detector. In order to make the sample conductive and avoid electric charge effect, the specimens were gold coated using an Emscope SC500 specimen vacuum gold coater and stored in a desiccator prior to analysis. A semi-quantitative analysis of sample inorganic components was conducted using energy-dispersive X-ray (EDX) spectroscopy system software integrated with a scanning electron microscope. X-ray diffraction (XRD) patterns were recorded using a Bruker D8 powder diffractometer system operating with a Cu Kα radiation source. The X-ray patterns were acquired by means of the DIFFRACPlus software and recorded in the 2θ range of 10–80°, with a step width of 0.033 and a time per step of 1 s. In order to identify the main crystalline phases for each sample, XRD patterns were matched to an X-ray diffraction pattern library using the software package Highscore (Panalytic, UK). Basic surface functionalities of materials were measured through Boehm titrations, using the method reported elsewhere [27]. In particular, one gram of each activated carbon was mixed with 50 mL of 0.05 M solutions of either sodium hydroxide (NaOH) or hydrochloric acid (HCl) in vials, which were sealed and shaken for 24 h. Solutions were previously standardized following the procedure suggested by Oickle et al. [28]. The content of the vials was filtered, and 5 mL of each filtrate was pipetted into a beaker. The excess of base or acid was then titrated with either HCl or NaOH, respectively. The amounts of basic and acidic surface groups were determined according to the relationships reported by Goertzen et al. [29] for direct titrations and given in the following equations:

$$\text{Basic} = \frac{[\text{HCl}] \cdot V_{\text{HCl,mix}} - ([\text{NaOH}] \cdot V_{\text{NaOH,cons}} \cdot \text{DF})}{m_{\text{carbon}}} \tag{1}$$

$$\text{Acidic} = \frac{[\text{NaOH}] \cdot V_{\text{NaOH, mix}} - ([\text{HCl}] \cdot V_{\text{HCl,cons}} \cdot \text{DF})}{m_{\text{carbon}}} \tag{2}$$

where, basic and acidic are the mmol of basic and acidic surface groups, respectively, per unit mass of carbon ($m_{\text{carbon}}$), [HCl] and [NaOH] are the concentration values of the standardized solutions, $V_{\text{HClmix}}$ and $V_{\text{NaOHmix}}$ are the volumes of the standardized solutions mixed with the carbon, $V_{\text{NaOHcons}}$ and $V_{\text{HClcons}}$ are the volumes of the standardized solutions consumed during titration and DF is a dilution factor equal to 10.

Results were interpreted according to the assumption that NaOH neutralizes all acidic groups (carboxylic, phenolic and lactonic groups) and HCl reacts with all basic groups.

*2.3. CO$_2$ Sorption Measurements*

CO$_2$ sorption capacities were measured on a Mettler Toledo thermogravimetric analyzer (TGA)/differential scanning calorimeter (DSC) [30]. Samples were initially degassed in N$_2$ (50 mL·min$^{-1}$) at 120 °C for 30 min. Materials were then cooled down to ca. 35 or 53 °C under N$_2$ prior to measuring CO$_2$ uptake. Gas atmosphere was then changed to pure CO$_2$ or 15% *v/v* CO$_2$ in N$_2$ (total 50 mL·min$^{-1}$), and temperature was held for 30 min in order to measure adsorption at a total pressure of 1 bar. Next, temperature was increased up to 100 °C at 5 °C·min$^{-1}$ to start desorbing CO$_2$. Regeneration was then completed by switching the atmosphere back to N$_2$ and further increasing temperature up to 120 °C. The latter temperature was held for 15 min. Flow rate was kept constant throughout the experiment. In addition, the recyclability of the best performing sample was tested over ten adsorption/desorption cycles. The same program was used, but in this case regeneration was accomplished in just a single step by heating the sample (at 5 °C·min$^{-1}$) to 120 °C under 15% CO$_2$. The atmosphere during desorption was kept the same as adsorption in order to simulate a rapid temperature swing adsorption (RTSA) as a regeneration strategy, where partial pressure is not changed.

## 3. Results and Discussion

Figure 2 and Table 2 reveal the absence of a porous structure for raw *Laminaria hyperborea*. A negligible surface area (<1 m$^2$·g$^{-1}$) was already reported for raw macroalgae waste (algal meal)

by Ferrera-Lorenzo et al. [31]. The pyrolytical treatment caused the development of a rudimentary porous structure, which was slightly enhanced after $CO_2$ activation. In contrast, KOH-activated carbon presented outstanding textural properties. The significant porosity development exhibited by KOH-treated char was attributed to the combined effect of the KOH activation mechanism (pore creation) and HCl washing (pore unblocking, i.e., removal of KOH activation residues filling the pores).
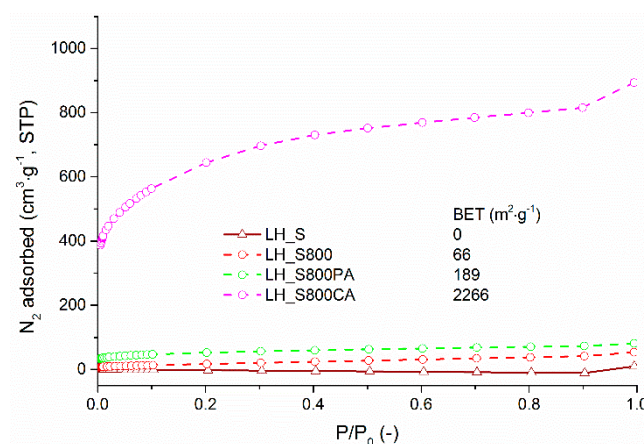


**Figure 2.** $N_2$ adsorption isotherms at 77 K for all samples.

**Table 2.** Textural parameters for all samples.

| Sample ID | $S_{BET}$ [a] $m^2 \cdot g^{-1}$ | $V_{tot}$ [b] $cm^3 \cdot g^{-1}$ | $V_{mi}$ [c] $cm^3 \cdot g^{-1}$ | $V_{me}$ [d] $cm^3 \cdot g^{-1}$ | $V_{ma}$ [e] $cm^3 \cdot g^{-1}$ |
|---|---|---|---|---|---|
| LH_S | 0 | 0.015 | 0.000 | 0.006 | 0.009 |
| LH_S800 | 66 | 0.083 | 0.021 | 0.039 | 0.024 |
| LH_S800PA | 189 | 0.126 | 0.069 | 0.030 | 0.028 |
| LH_S800CA | 2266 | 1.384 | 0.822 | 0.197 | 0.365 |
| MgO | 72 | 0.129 | 0.037 | 0.071 | 0.021 |

[a] Surface area calculated by applying the Brunauer–Emmett–Teller (BET) method [20] to $N_2$ adsorption data. [b] Total pore volume calculated by applying Gurvitsch's rule [22] at $P/P_0=0.99$. [c] Micropore volume calculated by applying the Dubinin–Radushkevich (DR) model [23] to $N_2$ adsorption data. [d] Mesopore volume calculated by applying the Barrett–Joyner–Halenda (BJH) model to $N_2$ adsorption data. [e] Macropore volume calculated by difference.

Figure 3a depicts the morphology of raw *Laminaria hyperborea*. This was typical of a plant tissue structure [32]. Carbonization and $CO_2$ activation processes did not significantly change the initial morphology of macroalgae (see Figure 3b,c). This agrees with the limited increase of porosity measured by gas sorption for LH_S800 and LH_S800PA (see Figure 2). SEM images at 5000x showed particles lying on the carbon substrate of LH_S800 and LH_S800PA. These particles were found to be inorganic based on the EDX chemical compositions corresponding to the SEM micrographs (see Figure 4). The fact that no inorganic particles were observed for LH_S800CA (see Figure 3d) is in agreement with the poorer inorganic fractions detected by EDX analysis for this sample (see Figure 4). As a result, an increase of the carbon abundance was measured for KOH-activated carbon. As already mentioned, the decrease in mineral matter was caused by HCl rinsing of KOH–AC, which promoted the development of porosity. Nonetheless, only macropores could be observed from Figure 3d as the scale did not allow for identification of smaller pores.
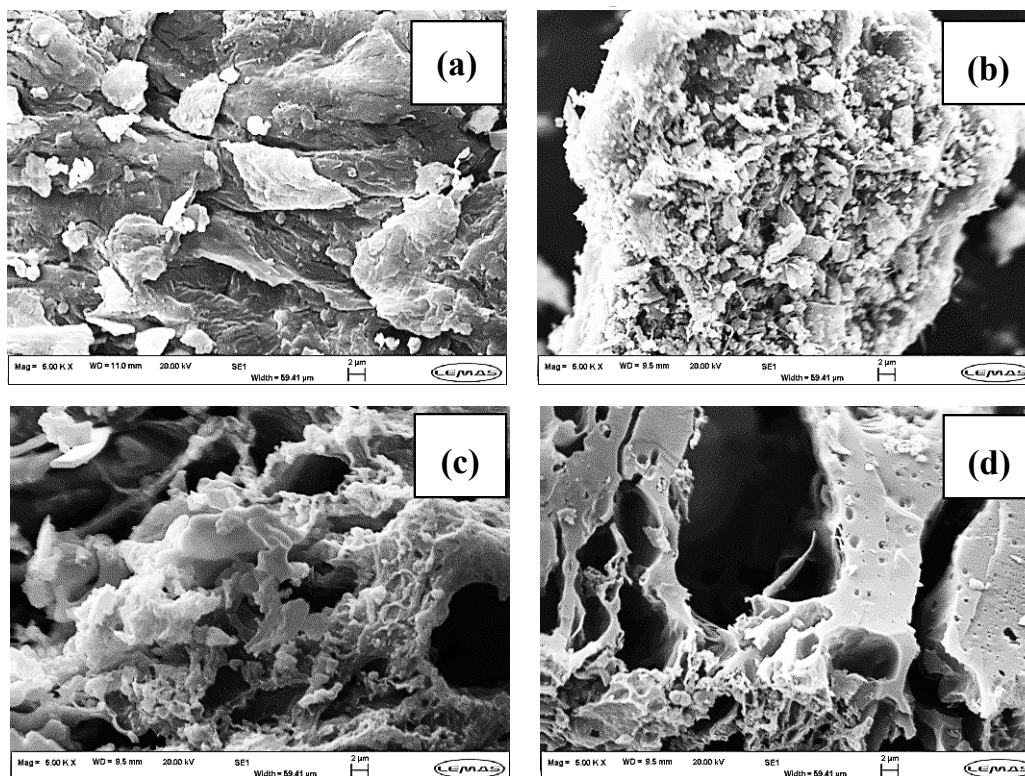
**Figure 3.** SEM images at 5000× magnification for (**a**) LH_S, (**b**) LH_S800, (**c**) LH_S800PA and (**d**) LH_S800CA.
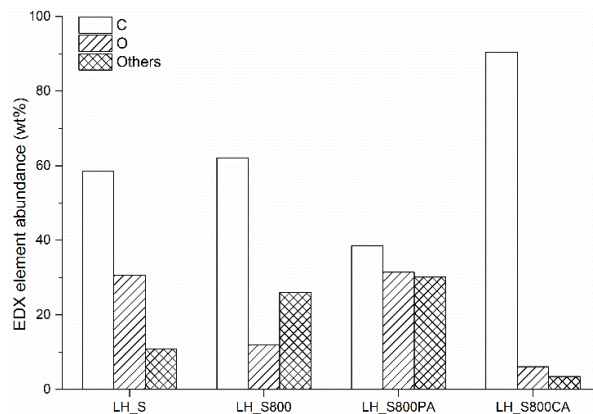


**Figure 4.** EDX chemical compositions corresponding to the SEM micrographs shown in Figure 3 for all samples.

Alkaline fractions were measured by AAS, ICP-OES and ICP-MS for all the samples, which are given in Table 3. The amount of alkali species present within raw *Laminaria*, pyrolyzed *Laminaria* and $CO_2$-activated carbon followed the sequence K>Na>Ca>Mg. This was consistent with ICP-MS results previously reported by Ross et al. [33]. After pyrolysis, the concentration of all alkali metals significantly increased. This was due to the devolatilization that occurred during pyrolytical treatment and was in agreement with proximate findings (see Table 4). Alkali metal concentration did not noticeably change following physical activation. On the other hand, chemical treatment, with particular regard to HCl rinsing, caused a dramatic decrease of all alkali species, especially for K and Na.

**Table 3.** Alkali metal concentration measured by atomic absorption spectroscopy (AAS), inductively coupled plasma optical emission spectrometry (ICP-OES), and inductively coupled plasma mass spectrometry (ICP-MS) for raw *Laminaria* (LH_S), pyrolyzed *Laminaria* (LH_S800), $CO_2$-activated char (LH_S800PA) and KOH-activated (LH_S800CA) char.

| AAS | | | | | | | |
|---|---|---|---|---|---|---|---|
| **LH_S** | | **LH_S800** | | **LH_S800PA** | | **LH_S800CA** | |
| **Elem** | **Ppm** | **Elem** | **Ppm** | **Elem** | **Ppm** | **Elem** | **Ppm** |
| Ca | 8.9E3 | Ca | 2.1E4 | Ca | 2.3E4 | Ca | 1.2E4 |
| K | 4.6E4 | K | 1.2E5 | K | 1.4E5 | K | 1.8E3 |
| Mg | 6.7E3 | Mg | 1.7E4 | Mg | 1.9E4 | Mg | 7.8E3 |
| Na | 2.8E4 | Na | 7.7E4 | Na | 7.9E4 | Na | n.d. |
| **ICP-OES** | | | | | | | |
| **LH_S** | | **LH_S800** | | **LH_S800PA** | | **LH_S800CA** | |
| **Elem** | **Ppm** | **Elem** | **Ppm** | **Elem** | **Ppm** | **Elem** | **Ppm** |
| Ca | 9.9E3 | Ca | 2.6E4 | Ca | 2.8E4 | Ca | 1.4E4 |
| K | 5.2E4 | K | 1.4E5 | K | 1.5E5 | K | 2.4E3 |
| Mg | 7.7E3 | Mg | 1.9E4 | Mg | 2.0E4 | Mg | 9.6E3 |
| Na | 2.9E4 | Na | 7.6E4 | Na | 7.9E4 | Na | n.d. |
| **ICP-MS** | | | | | | | |
| **LH_S** | | **LH_S800** | | **LH_S800PA** | | **LH_S800CA** | |
| **Elem** | **Ppm** | **Elem** | **Ppm** | **Elem** | **Ppm** | **Elem** | **Ppm** |
| Ca | 9.1E3 | Ca | 2.3E4 | Ca | 2.5E4 | Ca | 9.8E3 |
| K | 4.4E4 | K | 1.2E5 | K | 1.3E5 | K | 2.2E3 |
| Mg | 5.1E3 | Mg | 1.7E4 | Mg | 1.8E4 | Mg | 8.5E3 |
| Na | 2.7E4 | Na | 7.3E4 | Na | 7.7E4 | Na | n.d. |

Elem stands for element; n.d. stands for not detected.

**Table 4.** Elemental and proximate analyses for all samples.

| Sample ID | Ultimate, db | | | | Proximate, db | | |
|---|---|---|---|---|---|---|---|
| | **N** | **C** | **H** | **S** | **VM** | **A** | **FC** |
| LH_S | 1.7 | 40.1 | 5.3 | 0.3 | 77.7 | 18.1 | 4.2 |
| LH_S800 | 1.7 | 46.9 | 0.9 | 2.3 | 13.2 | 59.3 | 27.5 |
| LH_S800PA | 1.4 | 28.5 | 0.7 | 0.0 | 21.1 | 48.7 | 30.2 |
| LH_S800CA | 0.9 | 89.1 | 0.4 | 1.1 | 16.4 | 11.1 | 72.5 |

db stands for dry basis. VM stands for volatile matter. A stands for ash. FC stands for fixed carbon. Proximate analyses for LH_S and LH_S800 were carried out by British Standard Institute (BSI) methods [24–26]. Proximate analyses for LH_S800PA and LH_S800CA were carried out by thermogravimetric analysis (TGA).

As depicted in Figure 5a,b, XRD patterns measured for raw macroalgae (LH_S) and its pyrolyzed derivative (LH_S800) displayed the presence of a series of sharp and intense peaks. Most of the sharp peaks found for virgin *Laminaria* matched the standard pattern of potassium chloride (00-004-0587), which can be considered as the main crystalline phase for this sample. All peaks related to this phase were also detected in the XRD pattern of seaweed char. This was in line with the high content of K given in Table 3 for raw and pyrolyzed *Laminaria*. Most of the remaining peaks identified for LH_S were associated with sodium chloride (01-080-3939). All these peaks were also found in the pattern of pyrolyzed *Laminaria*, yet a slight shift toward lower angles was noticed. This might have been due to a distortion of the lattice parameter of the crystals.
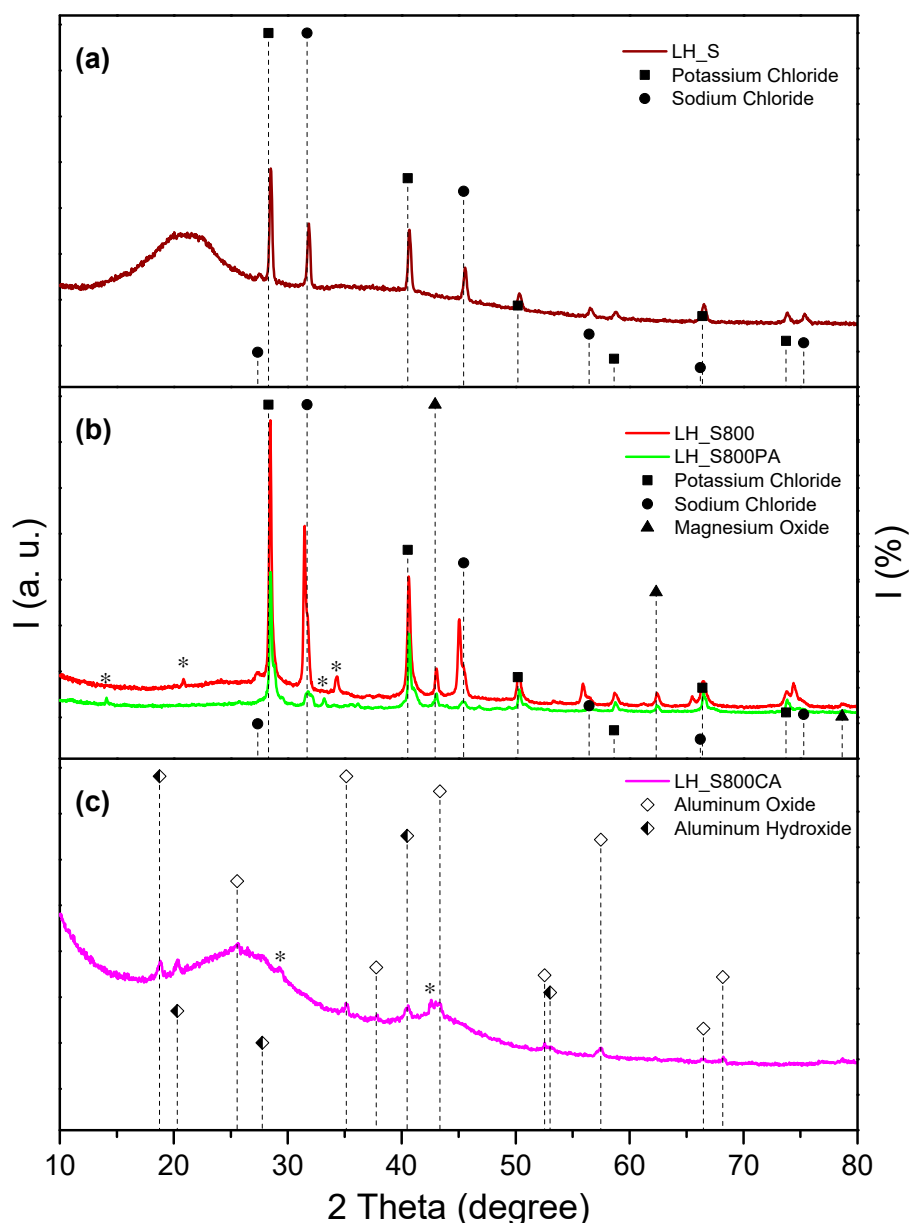
**Figure 5.** XRD patterns for (**a**) raw macroalgae (LH_S), (**b**) pyrolyzed macroalgae (LH_S800) and $CO_2$-activated counterpart (LH_S800PA) and (**c**) KOH-activated counterpart (LH_S800CA).

Crystalline phases detected in this study for virgin and carbonized seaweed agreed with results previously reported in the literature. In particular, Wang et al. [34] identified the presence of alkali chlorides within seaweed-based ash. In addition, sylvite (KCl) was detected on seaweed ash by Yaman et al. [35], while halite (NaCl) matched the pattern of oarweed-based chars obtained after pyrolysis at 500 °C [36]. Furthermore, reflections corresponding to halite were also found for raw seaweed (i.e., *Undaria pinnatifida*) by Song et al. [37]. The same phase was retained after pyrolysis at 1000 °C.

Interestingly, as observed in Figure 5b, additional signals were measured for pyrolyzed seaweed. This suggested the formation of new phases after pyrolysis treatment. In particular, reflections observed at ca. 43, 62 and 78° 2θ were assigned to magnesium oxide. This compound was also identified by Song et al. [37] after pyrolysis of seaweed (i.e., *Undaria pinnatifida*) at 1000 °C. According to the authors, magnesium ions may react with oxygen-containing species such as $H_2O$ to form MgO during pyrolysis at high temperature. In addition to this, as suggested by Ross et al. [33], most of the inorganic fractions contained in raw seaweed tend to decompose to their oxides when pyrolyzed at 750–800 °C.

Accordingly, it might also be the case that crystalline MgO arose from the pyrolytic breakdown of amorphous Mg alginates present within the raw brown algae [35]. Some residual peaks with low intensity measured at ca. 21 and 34° 2θ were ascribed to unknown impurities (see asterisks in Figure 5b). These reflections might be attributed to trace alkali metals or alkali-based alginates whose detection is prevented by overlapping with phases that are more dominant. Figure 5b also showed that all peaks identified within pyrolyzed *Laminaria* were observed for its $CO_2$-activated counterpart. This result confirms that inorganic phases were largely retained after $CO_2$ treatment. By contrast, as seen by Figure 5c, no peaks associated with alkali chlorides and magnesium oxides were found for LH_S800CA. This can be attributed to the dissolution of crystallites after acid washing, which is corroborated by EDX (see Figure 4), AAS/ICP-OES/ICP-MS (see Table 3) and proximate (see Table 4) results. However, a series of low intensity peaks were measured for LH_S800CA. Most of these were best fitted by the standard pattern of aluminum oxide (04-013-1687) and aluminum hydroxide (04-014-1754). Oxidized forms of Al seemed to be the only inorganic phases that were not fully dissolved by HCl washing. In addition to that, weak peaks related to other unknown impurities (see asterisks in Figure 5c) were observed at ca. 29 and 42° 2θ. These might be ascribed to trace alkali metals. Nevertheless, LH_S800CA's pattern also showed two broad peaks at around 25 (002) and 43° 2θ (100). These highlighted a more amorphous structure of the sample, typical of activated carbon [38]. Moreover, LH_S800CA's pattern suggested that after KOH activation, a decrease in long-range graphenic ordering in the carbon nanostructure (amorphization) occurred. The disordering mechanism induced by KOH activation in the nanostructure of pitch-derived carbonaceous materials was discussed by Król et al. [39]. This seems to have contributed to the generation of micropores in LHS_800CA, as also suggested in Table 2. However, the limited $CO_2$ capture potential measured for the KOH-activated material might suggest that the LHS_800CA nanostructure lacks narrow nanopores (diameter < 0.7 nm), which are those favoring $CO_2$ adsorption under post-combustion conditions [18,19].

A large number of basic groups (up to ca. 2.2 mmol·$g^{-1}$) was measured for pyrolyzed seaweed by Boehm titration. The significant concentration of basic functionalities could be associated with the high level of alkali metals present within the macroalgae char. Basic functionalities appeared to be entirely retained after $CO_2$ activation, whereas much lower basicity was found for the KOH activated char (see Figure S2, Supplementary Materials). Once again, this result is in line with EDX and proximate findings, and was due to the demineralization of the KOH-activated carbon following HCl rinsing.

When measuring $CO_2$ uptake at 35 °C and 1 bar (see Figure S3, Supplementary Materials), seaweed char and $CO_2$-activated counterpart exhibited slower kinetics and lower uptakes than those achieved by the KOH-activated sample. This suggests that surface area (and then physisorption) is a predominant feature of $CO_2$ capture process at low temperature and high partial pressure of $CO_2$.

The post-combustion capture performance of pyrolyzed *Laminaria* and its activated derivatives were compared, as seen in Figure 6. A commercial carbon (AR) and pure magnesium oxide (MgO) were included for comparison purposes. At lower partial pressure (0.15 bar) of $CO_2$ and higher temperature (53 °C), LH_S800CA and AR exhibited the fastest sorption kinetics. In spite of this, both KOH-activated and commercial carbon attained much lower sorption capacity than those measured for seaweed char and its $CO_2$-activated counterpart. In addition, the $CO_2$ sorption capacities recorded for LH_S800CA and AR were not steady but appeared to decrease over the equilibration time. The sorption behavior exhibited by LH_S800CA and AR was typical of physisorbents whose $CO_2$ capture mechanism only relies on weak bonds and becomes less effective at high temperature. Therefore, despite feed gas and adsorption temperature being kept constant throughout the adsorption process, the capacity loss measured for LH_S800CA and AR with increasing time could be reasonably attributed to the prolonged exposure of the materials at a relatively high temperature (53 °C), which appeared to have favored desorption of weakly bonded $CO_2$. Furthermore, LH_S800CA and AR are highly porous carbons, which are known to strongly retain water vapor within their pores. Considering that the materials were subjected to a mild drying (120 °C under $N_2$), it is likely the so dried sorbents still contained a significant amount of residual moisture, which might have hindered the $CO_2$ physisorption mechanism

onto their pores. Importantly, despite the very low surface area available, LH_S800 and LH_S800PA significantly outweighed the sorption performance of the KOH-activated carbon, capturing nearly twice as much $CO_2$ as that adsorbed by LH_S800CA after 30 min. The remarkable difference in surface area between the samples (see Figure 2) seems to suggest that textural properties did not play a key role (relative to alkali-based chemisorption) in the sorption potential exhibited by macroalgae char and its $CO_2$-activated derivative under typical post-combustion conditions (0.15 bar $CO_2$ and 53 °C temperature). In fact, as mentioned above, unlike for LH_S800CA, which was demineralized (i.e., HCl washing), a relatively high concentration of alkali metals was found for LH_S800, which was largely retained after $CO_2$ activation. HCl washing was not applied post $CO_2$-activation to preserve all alkali-based compounds within the LHS_800CA structure. If $CO_2$-activated carbons would have been washed with HCl, only physisorption would have occurred, thus reducing the efficiency of the material at absorbing $CO_2$, which might have ended up being lower than that exhibited by LHS_800CA. The inherent alkalinity of seaweed-char and its $CO_2$-activated product agreed with the higher number of basic groups measured for these samples compared to that of LH_S800CA (see Figure S2, Supplementary Materials). Note that the amount of basic groups measured for LH_S800PA was ca. 2.2 mmol·$g^{-1}$, whereas the $CO_2$ sorption capacity of the sample was only ca. 0.25 mmol·$g^{-1}$. Assuming that each mol of basic group captured one mol of $CO_2$, the discrepancy between the amount of basic groups and the $CO_2$ sorption capacity appears to indicate that not all the basic functionalities present on the sorbent were effective for $CO_2$ sorption. This suggests that the type of alkali metal-containing groups significantly affects the $CO_2$ capture process on macroalgae-derived sorbents.
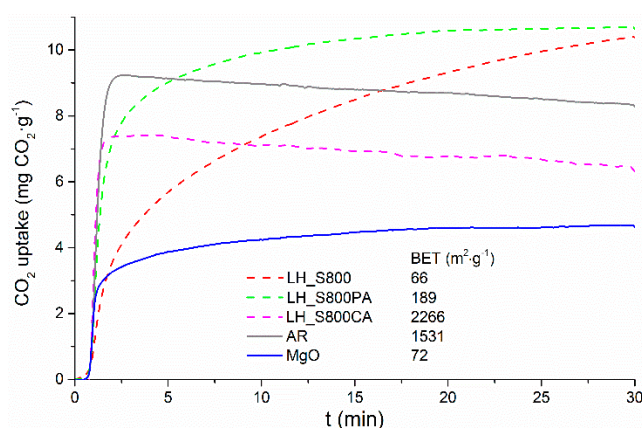


**Figure 6.** $CO_2$ adsorption kinetic at 53 °C and 0.15 bar (total pressure of 1 bar) measured for pyrolyzed macroalgae (LH_S800), $CO_2$-activated counterpart (LH_S800PA), KOH-activated counterpart (LH_S800CA), commercial carbon (AR) and magnesium oxide (MgO).

However, it seems that the effect of inorganic species on the sorption potential of LH_S800 and LH_S800PA becomes more influential at lower partial pressure, when a higher selectivity is vital. In particular, magnesium oxide, which was identified by XRD analyses onto the structure of pyrolyzed and $CO_2$-activated macroalgae (see Figure 5), may have been responsible for the (chemi)sorption of $CO_2$ under post-combustion conditions. As indicated by Figure 6, this assumption was corroborated by the $CO_2$ sorption kinetic measured for magnesium oxide under simulated post-combustion conditions, which appeared to mirror those observed for $CO_2$-activated *Laminaria* char (LH_S800PA). However, Figure 6 also shows that MgO exhibited lower $CO_2$ uptakes (4.6 mg $CO_2$·$g^{-1}$, i.e., ca. 0.105 mmol $CO_2$·$g^{-1}$) than that attained by LH_S800PA. Considering that adsorption conditions were common to all samples, the greater $CO_2$ sorption potential exhibited by the $CO_2$-activated *Laminaria* char might be ascribed to the higher physisorption contribution (larger surface area, see Figure 2) that occurred on the macroalgae-based carbon in comparison to that of pure magnesium oxide, whose $CO_2$ capture capacity was mostly due to chemisorption. Accordingly, LH_S800PA's capture potential seems to be the result of a synergetic effect of physisorption and chemisorption processes. By contrast, although the

macroalgae-based char (LH_S800) attained nearly as much $CO_2$ uptake as that achieved by LH_S800PA, the former exhibited a much slower uptake rate than the latter. This may be attributed to the less developed porous network featured by this sample (see Figure 2 and Table 2). This caused a reduced mobility of $CO_2$ through the pore channels of the material, and therefore a delay in accessing both the carbon pores (i.e., physisorption sites) and the MgO particles (i.e., chemisorption sites) present within the porous network of the material. Therefore, it seems that the more developed porous network exhibited by LH_S800PA not only ensured a higher physisorption effect, but might have also facilitated the access of $CO_2$ to the chemisorption sites (i.e., MgO crystals).

However, it is speculated that the $CO_2$ sorption performance of LH_S800 and LH_S800PA might also be due to the presence of an additional $CO_2$ chemisorption mechanism. Specifically, it might be that the heat-treatment of pristine macroalgae, containing a significant proportion of Na and K (see Table 3), led to the formation of potassium and/or sodium carbonate. As given by [8,13,14], Na and K-based carbonates can absorb $CO_2$ under moist conditions, giving rise to alkali metal bicarbonates. Therefore, assuming that some water molecules remained trapped within the structure of the materials after initial degassing at 120 °C for 30 min, this would explain the higher sorption capacity exhibited by *Laminaria*-derived sorbents in comparison to magnesium oxide.

Nevertheless, the highest sorption capacity exhibited by MgO-containing materials synthesized in this work (10.7 mg $CO_2 \cdot g^{-1}$ for LH_S800PA, see Figure 6) was lower than the capture capacity (63 mg $CO_2 \cdot g^{-1}$) achieved by a MgO-containing mesoporous carbon under similar conditions ($T_{ads}$ = 50 °C, $PCO_2$ = 0.15 bar) [15]. In spite of this, the synthesis of alkali metal-containing sorbents presented in this study was more sustainable and cheaper compared to that reported in the work of Bhagiyalakshmi et al. [15], as seaweed treatment was less energy demanding than the methodology applied by these authors. In addition to this, the fabrication process reported in this work did not involve any chemical addition (i.e., impregnation of alkali-containing compounds) and entailed the use of a widely available feedstock. Moreover, the best performing sorbent prepared in this work (LH_S800PA) was fully regenerated at lower temperature (100 °C, see Figure 7) than that applied by [15] (200 °C), which would imply a lower cost associated with RTSA cyclic operations. Interestingly, the regeneration temperature of MgO-containing carbon materials fabricated in this work was noticeably lower than that usually reported for pure MgO (450–500 °C) [15,40]. Bhagiyalakshmi et al. [15], who synthesized a magnesium oxide-containing carbon, explained this behavior through the weaker interaction between $CO_2$ and the MgO particles not embedded within the framework of the carbon-based sorbent. On the other hand, the facile regeneration exhibited by LH_S800PA appears to suggest that Na and K-based carbonates may be also contributing in the $CO_2$ capture process. In fact, the corresponding Na and K bicarbonates, possibly formed after $CO_2$ adsorption step, are less stable and can be easily regenerated at low temperature (100–200 °C).
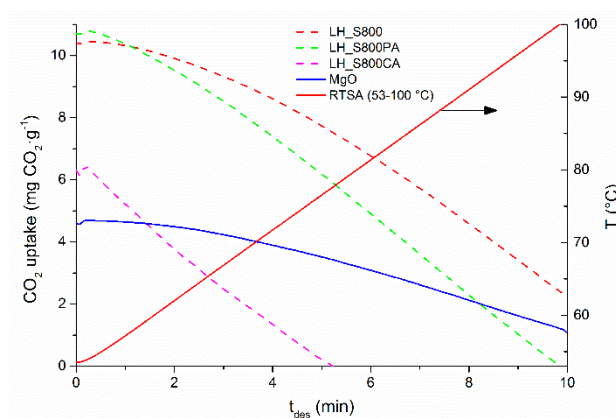


**Figure 7.** Regeneration (RTSA, 53–100 °C) for pyrolyzed macroalgae (LH_S800), $CO_2$-activated counterpart (LH_S800PA), KOH-activated counterpart (LH_S800CA) and magnesium oxide (MgO).

The easier regeneration (no $CO_2$ left at ca. 80 °C) exhibited by LH_S800CA in Figure 7 seems to indicate a weak (physi)sorption of $CO_2$ onto this sample. In contrast, LH_S800 and pure magnesium oxide appeared to be more difficult to regenerate, as indicated by the slower release of $CO_2$ with increasing time and the residual $CO_2$ retained within these samples at the end of the desorption step.

Hence, based on results earlier presented, a cyclic test under post-combustion conditions was performed for LH_S800PA only, as this was the most promising sample in terms of sorption potential, kinetics and regeneration capacity. In addition, in order to ensure full regeneration of the sorbent, it was decided to extend the temperature swing up to 120 °C when performing RTSA cycling as a regeneration strategy (see Figure 8a).
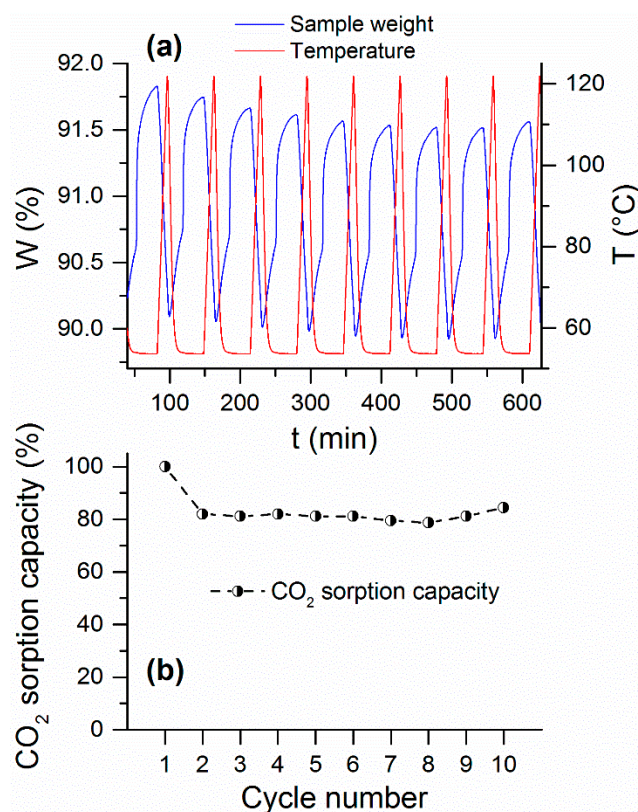


**Figure 8.** (**a**) Recyclability and (**b**) sorption capacity over ten RTSA cycles for LH_S800PA.

As depicted by Figure 8a, a relatively fast $CO_2$ uptake rate was observed for LH_S800PA, which was consistent with the sorption behavior displayed by this sample in Figure 6. Nonetheless, this sorbent appeared not to reach its maximum capacity at the end of the equilibration time, thereby indicating the potential of attaining even higher sorption capacity over a longer adsorption stage. Desorption of $CO_2$ was efficiently accomplished after increasing the temperature up to 120 °C. On the other hand, according to results displayed in Figure 7, this material could be regenerated at even lower temperature, thus reducing the cost of the regeneration step.

However, as shown in Figure 8b, a noticeable capacity loss (ca. 20%) occurred between cycle 1 and cycle 2. The decay of sorption capacity was presumably due to the incomplete reconversion of magnesium carbonate into MgO (e.g., formation of intermediates such as $Mg(OH)_2$), thus leading to a decrease of chemisorption potential. Yet, as highlighted by Figure 8b, the sorbent's capacity stabilized after the first cycle, thus indicating good durability over time. Note that the apparent decrease of the plateau illustrated in Figure 8a was due to a continuous baseline drift downwards.

## 4. Conclusions

The current work showed that *Laminaria hyperborea* processing led to a more sustainable, less costly and easier fabrication of alkali-based $CO_2$ sorbents compared to procedures previously reported in the literature, as no chemical addition (e.g., impregnation of alkali-containing species) was required. This was achieved by exploiting the advantageous chemistry of the widely available macroalgae, intrinsically containing high concentration of alkali metals within its structure.

Pyrolysis of raw material led to the formation of a char rich in ash (up to 59.3%) but with low carbon purity. Very large surface area (up to 2266 $m^2 \cdot g^{-1}$) was obtained after KOH activation of char, which implied the highest $CO_2$ uptake (up to nearly 60 mg $CO_2 \cdot g^{-1}$) at 35 °C and 1 bar. Interestingly, despite the undeveloped porous structure, pyrolyzed *Laminaria* (LH_S800) and its $CO_2$-activated counterpart (LH_S800PA) exhibited a far greater sorption potential than that measured for the KOH-activated sample (LH_S800CA) and a commercial carbon (AR) under simulated post-combustion conditions (53 °C and 0.15 bar). This result was ascribed to the chemisorption contribution given by the alkali metal-based species present within the structure of macroalgae-derived char and $CO_2$-activated derivative. The inherent alkalinity nature of the LH_S800 and LH_S800PA was corroborated by the higher number of basic surface functionalities measured through Boehm titrations compared to those found onto the surface of LH_S800CA. This was associated with the removal of mineral matter that occurred after KOH treatment (i.e., KOH activation followed by HCl washing) of macroalgae char.

Observations revealed that alkalinity-based chemisorption was dominant at higher temperatures and lower $CO_2$ partial pressures, while surface-based physisorption was dominant at lower temperatures and higher $CO_2$ partial pressures. In particular, magnesium oxide was identified by XRD within the structure of seaweed char and its $CO_2$-activated counterpart. MgO crystals appeared to play a key role in the sorption of $CO_2$ at lower partial pressure and higher temperature. This was suggested by the similar sorption kinetics observed for pure magnesium oxide and LH_S800PA during the post-combustion test. However, $CO_2$ sorption capacity measured for $CO_2$-activated *Laminaria* char was higher than that observed for magnesium oxide. This was ascribed to a synergistic effect of physisorption (more developed porous network) and chemisorption contributions occurring onto LH_S800PA. On the other hand, it is also ventured that Na and K-based carbonates, possibly present within the structure of the *Laminaria*-derived sorbent, might have also contributed to the capture of $CO_2$.

Although LH_S800 and LH_S800PA attained similar uptakes at saturation, the $CO_2$ sorption performance was optimized after $CO_2$ activation. In fact, LH_S800PA not only retained the same alkali metal-containing basic functionalities (i.e., magnesium oxide) originally present onto the char, but also had a more developed porous network. This seemed to have promoted the physisorption of $CO_2$ onto the carbon pores as well as the migration of $CO_2$ toward the chemisorption sites (MgO crystals), thereby implying an increase of the sorption speed. Moreover, the $CO_2$-activated carbon manifested a good durability and a more facile regeneration compared to the macroalgae char, which was accomplished at very low temperature (100 °C). Desorption temperature was much lower than that normally applied for similar alkali-based sorbents, thereby indicating promising and less expensive recyclability of this material.

The highest $CO_2$ sorption capacity (ca. 0.25 $mmol \cdot g^{-1}$) measured for the best performing material synthesized in this work (LH_S800PA) is lower than that (ca. 1.25 $mmol \cdot g^{-1}$ [41]) of the state of the art technology (30% MEA solution). Nevertheless, the $CO_2$ capture capacity of this class of sorbents may be potentially optimized by tuning the material properties (i.e., porosity, amount of alkali metal-based effective functionalities for $CO_2$ sorption). Furthermore, the presence of moisture in the post-combustion flue gas (not considered in this study) is believed to catalyze the reaction of Na/K carbonates (possibly present within the structure of LH_S800PA) with $CO_2$ to form the corresponding bicarbonates. Accordingly, this would improve both the $CO_2$ adsorption and desorption (regeneration) performance of the macroalgae-based sorbent. Therefore, future work should be carried out to systematically assess the influence of water vapor on the $CO_2$ sorption mechanism of the

seaweed-based activated carbons. In addition to this, the application of seaweed-derived solid $CO_2$ sorbents is more eco-friendly than absorption onto liquid amines, and the facile regeneration exhibited by macroalgae-based materials could potentially imply a lower energy penalty to the power plant than that caused by the regeneration of 30% MEA solution.

**Supplementary Materials:** The following are available online at http://www.mdpi.com/2673-4079/1/1/3/s1: Table S1: Details about inorganic elements detected by EDX analyses for all samples, Table S2: $CO_2$ uptakes at a total pressure of 1 bar, Table S3: Yields obtained for LH_800, LH_S800PA and LH_S800CA, Figure S1: Alkali metal concentration measured by atomic absorption spectroscopy (AAS), inductively coupled plasma optical emission spectrometry (ICP-OES) and inductively coupled plasma mass spectrometry (ICP-MS) for raw *Laminaria* (LH_S), pyrolyzed *Laminaria* (LH_S800), $CO_2$-activated char (LH_S800PA) and KOH-activated (LH_S800CA) char, Figure S2: Basic functionalities measured by Boehm's titration for pyrolyzed macroalgae (LH_S800), $CO_2$-activated counterpart (LH_S800PA) and KOH-activated counterpart (LH_S800CA), Figure S3: $CO_2$ adsorption kinetic at 35 °C and 1 bar (total pressure of 1 bar) for pyrolyzed macroalgae (LH_S800), $CO_2$-activated counterpart (LH_S800PA) and KOH-activated counterpart (LH_S800CA).

## References

1. Quadrelli:, R.; Peterson, S. The energy–climate challenge: Recent trends in $CO_2$ emissions from fuel combustion. *Energy Policy* **2007**, *35*, 5938–5952. [CrossRef]

2. Dhillon, R.S.S.; von Wuehlisch, G. Mitigation of global warming through renewable biomass. *Biomass Bioenergy* **2013**, *48*, 75–89. [CrossRef]

3. Rao, A.B.; Rubin, E.S. A Technical, Economic, and Environmental Assessment of Amine-Based $CO_2$ Capture Technology for Power Plant Greenhouse Gas Control. *Environ. Sci. Technol.* **2002**, *36*, 4467–4475. [CrossRef] [PubMed]

4. Plaza, M.G.; García, F.; Pis Rubiera, J.J.; Pevida, C. Post-combustion $CO_2$ capture with a commercial activated carbon: Comparison of different regeneration strategies. *Chem. Eng. J.* **2010**, *163*, 41–47. [CrossRef]

5. Yang, H.; Xu, Z.; Fan, M.; Gupta, R.; Slimane, R.B.; Bland, A.E.; Wright, I. Progress in carbon dioxide separation and capture: A review. *J. Environ. Sci.* **2008**, *20*, 14–27. [CrossRef]

6. Spigarelli, B.; Kawatra, S.K. Opportunities and challenges in carbon dioxide capture. *J. CO2 Utilizat.* **2013**, *1*, 69–87. [CrossRef]

7. Do, D.D.; Wang, K. A new model for the description of adsorption kinetics in heterogeneous activated carbon. *Carbon* **1998**, *36*, 1539–1554. [CrossRef]

8. Samanta, A.; Zhao, A.; Shimizu, G.K.; Sarkar, P.; Gupta, R. Post-Combustion $CO_2$ Capture Using Solid Sorbents: A Review. *Ind. Eng. Chem. Res.* **2012**, *51*, 1438–1463. [CrossRef]

9. Merkel, T.C.; Lin, H.; Wei, X.; Baker, R. Power plant post-combustion carbon dioxide capture: An opportunity for membranes. *J. Membr. Sci.* **2010**, *359*, 126–139. [CrossRef]

10. Wang, J.; Chen, H.; Zhou, H.; Liu, X.; Qiao, W.; Long, D.; Ling, L. Carbon dioxide capture using polyethylenimine-loaded mesoporous carbons. *J. Environ. Sci.* **2013**, *25*, 124–132. [CrossRef]

11. Gibson, J.A.; Gromov, A.V.; Brandani, S.; Campbell, E.E. The effect of pore structure on the $CO_2$ adsorption efficiency of polyamine impregnated porous carbons. *Microporous Mesoporous Mater.* **2015**, *208*, 129–139. [CrossRef]

12. Sayari, A.; Belmabkhout, Y. Stabilization of Amine-Containing $CO_2$ Adsorbents: Dramatic Effect of Water Vapor. *J. Am. Chem. Soc.* **2010**, *132*, 6312–6314. [CrossRef] [PubMed]

13. Zhao, C.; Chen, X.; Anthony, E.J.; Jiang, X.; Duan, L.; Wu, Y.; Dong, W.; Zhao, C. Capturing $CO_2$ in flue gas from fossil fuel-fired power plants using dry regenerable alkali metal-based sorbent. *Prog. Energy Combust. Sci.* **2013**, *39*, 515–534. [CrossRef]

14. Lee, J.B.; Ryu, C.K.; Baek, J.I.; Lee, J.H.; Eom, T.H.; Kim, S.H. Sodium-Based Dry Regenerable Sorbent for Carbon Dioxide Capture from Power Plant Flue Gas. *Ind. Eng. Chem. Res.* **2008**, *47*, 4465–4472. [CrossRef]

15. Bhagiyalakshmi, M.; Hemalatha, P.; Ganesh, M.; Mei, P.M.; Jang, H.T. A direct synthesis of mesoporous carbon supported MgO sorbent for $CO_2$ capture. *Fuel* **2011**, *90*, 1662–1667. [CrossRef]

16. Lee, S.C.; Chae, H.J.; Lee, S.J.; Choi, B.Y.; Yi, C.K.; Lee, J.B.; Ryu, C.K.; Kim, J.C. Development of Regenerable MgO-Based Sorbent Promoted with K2CO3 for $CO_2$ Capture at Low Temperatures. *Environ. Sci. Technol.* **2008**, *42*, 2736–2741. [CrossRef]

17. Ding, S.; Liu, Y. Adsorption of $CO_2$ from flue gas by novel seaweed-based KOH-activated porous biochars. *Fuel* **2020**, *260*, 116382. [CrossRef]

18. Zeng, G.; Lou, S.; Ying, H.; Wu, X.; Dou, X.; Ai, N.; Wang, J. Preparation of microporous carbon from Sargassum horneri by hydrothermal carbonization and KOH activation for $CO_2$ capture. *J. Chem.* **2018**, *2018*, 4319149. [CrossRef]

19. Balahmar, N.; Al-Jumialy, A.S.; Mokaya, R. Biomass to porous carbon in one step: Directly activated biomass for high performance $CO_2$ storage. *J. Mater. Chem. A* **2017**, *5*, 12330–12339. [CrossRef]

20. Brunauer, S.; Emmett, H.; Teller, E. Adsorption of Gases in Multimolecular Layers. *J. Am. Chem. Soc.* **1938**, *60*, 309–319. [CrossRef]

21. International Organization for Standardization. Technical Committee ISO/TC 24. Particle characterization including sieving, Subcommittee SC 4, Particle characterization. In *Determination of the Specific Surface Area of Solids by Gas Adsorption: BET Method*; ISO: Geneva, Switzerland, 2010; p. 24.

22. Plaza, M.G.; Pevida, C.; Arias, B.; Casal, M.D.; Martín, C.F.; Fermoso, J.; Rubiera, F.; Pis, J.J. Different Approaches for the Development of Low-Cost $CO_2$ Adsorbents. *J. Environ. Eng.* **2009**, *135*, 426–432. [CrossRef]

23. Dubinin, M.M.; Radushkevich, L.V. Equation of the characteristic curve of activated charcoal. *Chem. Zentr.* **1947**, *1*, 875–890.

24. EN, BS. *14775: 2009. Solid Biofuels–Determination of Ash Content*; British Standards Institution: London, UK, 2009.

25. EN, BS. *15148. Solid biofuels. Determination of the Content of Volatile Matter*; British Standards Institute: London, UK, 2009.

26. ISO, BSEN. *18134-3. Solid Biofuels—Determination in Moisture Content—Oven Dry Method—Part 3: Moisture in General Analysis Sample*; British Standards Institution: Bonn, Germany, 2015; pp. 1–14.

27. Bagreev, A.; Menendez, J.A.; Dukhno, I.; Tarasenko, Y.; Bandosz, T.J. Bituminous coal-based activated carbons modified with nitrogen as adsorbents of hydrogen sulfide. *Carbon* **2004**, *42*, 469–476. [CrossRef]

28. Oickle, A.M.; Goertzen, S.L.; Hopper, K.R.; Abdalla, Y.O.; Andreas, H.A. Standardization of the Boehm titration: Part II. Method of agitation, effect of filtering and dilute titrant. *Carbon* **2010**, *48*, 3313–3322. [CrossRef]

29. Goertzen, S.L.; Thériault, K.D.; Oickle, A.M.; Tarasuk, A.C.; Andreas, H.A. Standardization of the Boehm titration. Part, I. $CO_2$ expulsion and endpoint determination. *Carbon* **2010**, *48*, 1252–1261. [CrossRef]

30. Plaza, M.; Pevida, C.; Arias, B.; Fermoso, J.; Arenillas, A.; Rubiera, F.; Pis, J. Application of thermogravimetric analysis to the evaluation of aminated solid sorbents for $CO_2$ capture. *J. Therm. Anal. Calorim.* **2008**, *92*, 601–606. [CrossRef]

31. Ferrera-Lorenzo, N.; Fuente, E.; Suárez-Ruiz, I.; Ruiz, B. KOH activated carbon from conventional and microwave heating system of a macroalgae waste from the Agar–Agar industry. *Fuel Process. Technol.* **2014**, *121*, 25–31. [CrossRef]

32. Ferrera-Lorenzo, N.; Fuente, E.; Suárez-Ruiz, I.; Ruiz, B. Sustainable activated carbons of macroalgae waste from the Agar–Agar industry. Prospects as adsorbent for gas storage at high pressures. *Chem. Eng. J.* **2014**, *250*, 128–136. [CrossRef]

33. Ross, A.B.; Hall, C.; Anastasakis, K.; Westwood, A.; Jones, J.M.; Crewe, R.J. Influence of cation on the pyrolysis and oxidation of alginates. *J. Anal. Appl. Pyrolysis* **2011**, *91*, 344–351. [CrossRef]

34. Wang, S.; Jiang, X.M.; Wang, N.; Yu, L.J.; Li, Z.; He, P.M. Fusing characteristic analysis on seaweed biomass ash. *Zhongguo Dianji Gongcheng Xuebao/Proc. Chin. Soc. Electr. Eng.* **2008**, *28*, 96–101.

35. Haykiri-Acma, H.; Yaman, S.; Kucukbayrak, S. Production of biobriquettes from carbonized brown seaweed. *Fuel Process. Technol.* **2013**, *106*, 33–40. [CrossRef]

36. Stratford, J.P.; Hutchings, T.R.; de Leij, F.A. Intrinsic activation: The relationship between biomass inorganic content and porosity formation during pyrolysis. *Bioresour. Technol.* **2014**, *159*, 104–111. [CrossRef] [PubMed]

37. Song, M.Y.; Park, H.Y.; Yang, D.S.; Bhattacharjya, D.; Yu, J.S. Seaweed-Derived Heteroatom-Doped Highly Porous Carbon as an Electrocatalyst for the Oxygen Reduction Reaction. *ChemSusChem* **2014**, *7*, 1755–1763. [CrossRef] [PubMed]

38. Omri, A.; Benzina, M.; Ammar, N. Preparation, modification and industrial application of activated carbon from almond shell. *J. Ind. Eng. Chem.* **2013**, *19*, 2092–2099. [CrossRef]

39. Król, M.; Gryglewicz, G.; Machnikowski, J. KOH activation of pitch-derived carbonaceous materials—Effect of carbonization degree. *Fuel Process. Technol.* **2011**, *92*, 158–165. [CrossRef]

40. Wang, S.; Yan, S.; Ma, X.; Gong, J. Recent advances in capture of carbon dioxide using alkali-metal-based oxides. *Energy Environ. Sci.* **2011**, *4*, 3805–3819. [CrossRef]

41. Qi, G.; Fu, L.; Giannelis, E.P. Sponges with covalently tethered amines for high-efficiency carbon capture. *Nat. Commun.* **2014**, *5*, 1–7. [CrossRef]